



**Collective and Contractile Filament Motions in the Myosin Motility Assay**

Journal:	<i>Soft Matter</i>
Manuscript ID	SM-ART-10-2019-002082.R1
Article Type:	Paper
Date Submitted by the Author:	28-Dec-2019
Complete List of Authors:	Jung, Wonyeong; Purdue University, Weldon School of Biomedical Engineering Fillenwarth, Luke; Purdue University, Weldon School of Biomedical Engineering Matsuda, Atsushi; University of California Berkeley, Department of Mechanical Engineering Li, Jing; Purdue University, Weldon School of Biomedical Engineering Inoue, Yasuhiro; Kyoto University, Department of Micro Engineering Kim, Taeyoon; Purdue University, Weldon School of Biomedical Engineering; Purdue University System,

## **Collective and Contractile Filament Motions in the Myosin Motility Assay**

Wonyeong Jung<sup>1,§</sup>, Luke A. Fillenwarth<sup>1,§</sup>,  
Atsushi Matsuda<sup>2</sup>, Jing Li<sup>1</sup>, Yasuhiro Inoue<sup>3,\*</sup>, Taeyoon Kim<sup>1,\*</sup>

<sup>1</sup> Weldon School of Biomedical Engineering, Purdue University  
206 S. Martin Jischke Drive, West Lafayette, IN 47907, USA

<sup>2</sup> Department of Mechanical Engineering, University of California, Berkeley  
6141 Etcheverry Hall, Berkeley, CA 94720, USA

<sup>3</sup> Department of Micro Engineering, Kyoto University  
Kyotodaigaku-Katsura, Kyoto 615-8540, Japan

“§” indicates equal contribution

“\*” indicates corresponding author

## ABSTRACT

Cells require mechanical forces for their physiological functions. The forces are generated mainly from molecular interactions between actin filaments, cross-linking proteins, and myosin motors in the actin cytoskeleton. To better understand the molecular interactions, many studies employed myosin motility assays with actin filaments propelled by myosin heads fixed on a surface. Various interesting behaviors of actin filaments have been observed in the motility assay experiments. Despite the popularity of the motility assays, there were only a few computational models designed for simulating the motility assay systems. Most of the previous models have limitations which precluded full understanding of molecular origins for behaviors of actin filaments. In this study, we used an agent-based computational model based on Brownian dynamics for simulating the motility assay system. Our model rigorously describes the mechanics, dynamics, and interactions of actin filaments, cross-linking proteins, and molecular motors. Using the model, we first investigated how properties of actin filaments and motors affect gliding motions of actin filaments without volume-exclusion effects as a base study. We found that actin filaments can continuously glide at relative fast speed only when they are sufficiently longer than average spacing between neighboring motors and that the gliding speed of F-actins shows a biphasic dependence on processivity of motors. Then, we showed that volume-exclusion effects between actin filaments can induce diverse collective movements and alignment of actin filaments, thus creating thick bundles and ring-like structures in the absence of cross-linking proteins. Lastly, we demonstrated that cross-linking proteins can lead to distinct contractile behaviors of actin networks depending on the density and kinetics of the cross-linking proteins. Results from our study show the ability of our model to simulate the motility assay system under various conditions and provide insights into understanding of different behaviors of actin filaments.

## INTRODUCTION

The actin cytoskeleton within animal cells is responsible for a variety of functions. Interactions between F-actin, actin cross-linking protein (ACP), and molecular motors within the cytoskeleton generate mechanical forces that regulate physiological functions, such as cell migration, cytokinesis, wound healing, and morphogenesis.<sup>1, 2</sup> It is known that F-actins in cells carry tensile forces that are generated due to myosin motor proteins interacting with the F-actins. Dimers of myosin II assemble themselves into thick filaments. These thick filaments then walk toward the barbed end of the F-actin by using their motor heads.<sup>3</sup> This walking is often explained by the cross-bridge cycle with multiple states.<sup>4</sup> The transitions between these states are described by their mechanochemical rates.<sup>4</sup>

In vitro myosin motility assays have been used in the past to better study the interactions between F-actin and myosins. In these motility assays, F-actins move along a surface covered with immobilized myosin motor heads.<sup>5, 6</sup> When F-actin density is high in the presence of strong crowding effects, ordered motions of F-actins were observed. This is attributed to severe volume-exclusion effects between F-actins.<sup>7-11</sup> Above critical F-actin density, F-actins moved together as clusters, interconnected bands, and swirls. When ACPs were present, these motions became more or less collective.<sup>12-14</sup> For example, inclusion of fascin in the motility assay resulted in formation of rings, elongated fibers, and polar structures depending on conditions. However,  $\alpha$ -actinin led to contractile patches, and filamin A induced formation of a more stable network. Other ACPs, such as  $\alpha$ -EPLIN, cortexillin, and anillin, also induced formation of unique structures. Some of these studies suggested hypotheses about how interactions between F-actin, ACP, and myosin motors facilitate collective motions at both filament and network levels.

To provide more insights into understanding of microscopic origins, myosin motility assays have been also studied via computational and theoretical models. One study employed a stochastic model to show how twirling motions of F-actins are caused by myosin motors.<sup>15</sup>

An agent-based model based on Brownian dynamics was developed to determine an expression that can accurately predict how long gliding F-actins remain bound to myosin motors before dissociation.<sup>16</sup> Another model based on Brownian dynamics modeled F-actins as worm-like chains and cross-linkers and motors as springs with force-dependent kinetics.<sup>17</sup> This model demonstrated that the persistency and velocity of a gliding filament increase as a larger number of motors are bound to the filament due to an increase in either motor density, motor duty ratio, or filament length. In addition, a bead-rod model was employed to simulate single F-actin interacting with stationary motors simplified by springs.<sup>18</sup> This model demonstrated that higher ATP concentration leads to faster F-actin movement, whereas a change in motor density does not affect F-actin speed. Also, this study demonstrated that the gliding motion can be guided by chemical cues at probability directly affected by processivity of myosin motors. However, most of the previous models had limitations. For example, to reduce computational costs, the mechanics of F-actin was drastically simplified, or motors were considered implicitly by directly applying propelling forces to F-actin. In studies with explicit consideration of motors, gliding motion of only one F-actin was simulated, or mechanochemical cycles of myosin were not incorporated in a rigorous manner. Due to these critical limitations, it is difficult to rigorously investigate collective and contractile behaviors of multiple F-actins or how they emerge from molecular interactions between motors and F-actins.

To overcome these hurdles, we employed a well-established agent-based computational model based on Brownian dynamics with the Langevin equation.<sup>19, 20</sup> First, we ran simulations in the absence of ACPs and volume-exclusion effects between F-actins to focus on pure gliding motions of individual F-actins as a base study. We evaluated effects of a variation in the average length of F-actin and the density and mechanochemical rate of motors. Then, we investigated influences of volume-exclusion effects between F-actins on behaviors of F-actins by varying the strength of volume-exclusion effects acting between neighboring F-

actins. Lastly, we added ACPs with a wide range of density and unbinding rates to identify the effects of ACPs on contractile behaviors of F-actins in the motility assay.

## **METHODS**

### **Model overview**

An agent-based computational model based on Brownian dynamics was used, as in our previous studies.<sup>19-22</sup> In the model, F-actin, motor, and ACP are coarse-grained by cylindrical segments (Fig. S1a). Motions of the cylindrical segments representing F-actin and motor are updated using the Langevin equation, whereas motors are fixed in space to mimic the motility assay. Extensional and bending forces maintain equilibrium distances and angles formed by cylindrical segments. A repulsive force accounts for volume-exclusion effects between overlapping actin segments. Actin undergoes nucleation and polymerization events to form F-actin. ACPs attach to F-actin at a constant rate and can unbind from F-actin in a force-dependent manner following Bell's law.<sup>23</sup> Details of these features are explained in Supporting Information, and all parameter values are listed in Tables S1 and S2. Most of the parameter values are inherited from our previous models that successfully recapitulated various mechanical and dynamic behaviors of actin networks.<sup>19-22</sup> Values of particularly important parameters related to dynamic behaviors of ACPs and motors are determined based on experimental measurements or theoretical models as explained below. Parameter values in the range investigated in this study are not always physiologically relevant. Rather, as done in various *in vitro* studies, we aim to show the effects of variations in important parameter values over a wide range on behaviors of F-actins and networks to provide insights.

### **Dynamic behaviors of motors**

In this model, it is assumed that a motor arm represents cooperative behaviors of a small number of myosin heads in terms of kinetic behaviors. To avoid confusion, we name it one-arm motors rather than one-headed motors. Each motor arm can bind only to one binding

site on actin segments at a rate of  $40N_h \text{ s}^{-1}$ , where  $N_h$  is the number of myosin heads represented by each motor arm. We assume  $N_h = 8$ , resulting in slightly more processive motors and higher stall forces, as opposed to one myosin head in general. Walking ( $k_{w,M}$ ) and unbinding rates ( $k_{u,M}$ ) of the motor arms are determined by the parallel cluster model (PCM) to reflect the mechanochemical cycle of myosin motors.<sup>24, 25</sup> In the PCM, three mechanochemical states are defined, and there are five mechanochemical rates between the states (Table S2). Details of implementation and benchmarking of the PCM in our model were explained in detail in our previous study.<sup>19</sup> We vary one of the mechanochemical rates, ATP-dependent unbinding rate of myosin heads ( $k_{20}$ ), to probe its influences.  $k_{w,M}$  and  $k_{u,M}$  generated by PCM are proportional to  $k_{20}$  and lower with higher applied force, regardless of  $k_{20}$ ,<sup>26, 27</sup> which corresponds to the catch-bond behavior of myosin motors. The stall force is inversely proportional to  $k_{20}$ . Although we used the value of  $N_h$  higher than 1, the ranges of  $k_{w,M}$ ,  $k_{u,M}$ , and stall force explored in this study enable us to account for more or less processive motors. With the reference value of  $k_{20} = 20 \text{ s}^{-1}$ , the unloaded walking velocity of motors is 140 nm/s. This value is similar to the walking velocity of non-muscle myosin II,<sup>28, 29</sup> whereas it is  $\sim 2 \mu\text{m/s}$  with the highest value of  $k_{20}$  used in this study, which is larger than the walking velocity of smooth muscle myosin II.<sup>28, 30</sup>

### Initial simulation setup

We used a thin computational domain ( $10 \times 10 \times 0.1 \mu\text{m}$ ) with a periodic boundary condition in the x and y directions (Fig. S1b). F-actins are formed by the self-assembly of actin segments located at the same z position. ACPs are included only in a portion of the simulations. ACPs bind to F-actin to form functional cross-links between pairs of F-actins. Motors are distributed at random x and y coordinates at the same z position. A difference between z positions of F-actins and motors corresponds to the equilibrium length of motor arms (= 13.5 nm). Therefore, binding of a motor arm to F-actin is possible if they are located at similar x

and y coordinates. While F-actins are assembled, a fraction of the motor arms binds to F-actin with no walking motion. After all F-actins are assembled, motors start walking toward the barbed ends of F-actins.

### Quantification of F-actin motions

Velocities of endpoints of all actin segments,  $\mathbf{v}_{i,A}(t)$ , are calculated every two seconds. We quantified the distribution of  $|\mathbf{v}_{i,A}|$  measured at all time points to show speed distribution of all F-actins. To evaluate how fast F-actins are displaced by motors on average, the average speed of F-actins for each simulation is obtained by averaging  $|\mathbf{v}_{i,A}|$  over all endpoints and all time points.

In addition, persistency of motions of F-actins is evaluated by calculating the average of autocorrelation of velocity vectors:

$$\langle \cos \phi(\tau) \rangle = \left\langle \frac{2}{T-\tau} \sum_{t=0}^{(T-\tau)/2} \frac{\mathbf{v}_{i,A}(2t) \cdot \mathbf{v}_{i,A}(2t+\tau)}{|\mathbf{v}_{i,A}(2t)| |\mathbf{v}_{i,A}(2t+\tau)|} \right\rangle \quad (1)$$

where  $T$  is the duration of simulations, and  $\tau$  is time lag. If F-actins hardly change a direction during displacement for  $\tau$ ,  $\langle \cos \phi(\tau) \rangle$  is close to 1. In cases with F-actins propelled only by motors,  $\langle \cos \phi(\tau) \rangle$  exponentially decays.

We also evaluated the extent of collective motions by measuring a correlation between velocities of endpoints located on neighboring F-actins. As shown in previous studies, F-actins can exhibit collective motions by aligning with each other if there is a volume-exclusion effect between neighboring F-actins. During such collective motions, F-actins tend to move in a parallel or anti-parallel manner to avoid frequent collisions. For this calculation, we identify all pairs of endpoints on F-actins located at a distance between  $r$  and  $r + \Delta r$  and then calculate the average of correlations between velocities of all pairs:

$$\langle \cos \alpha(r, t) \rangle = \left\langle \frac{\mathbf{v}_{i,A}(t) \cdot \mathbf{v}_{j,A}(t)}{|\mathbf{v}_{i,A}(t)| |\mathbf{v}_{j,A}(t)|} \right\rangle \quad (2)$$

where  $\alpha$  is an angle between two velocity vectors, and the pair of endpoints  $i$  and  $j$  satisfies  $r \leq |\mathbf{r}_{i,A}(t) - \mathbf{r}_{j,A}(t)| < r + \Delta r$ , and they should not belong to the same F-actin. This calculation is performed for different  $r$  and  $t$  to measure the extent of collective motions of F-actins as a function of distance and time. Then, we calculated the time-averaged value of  $\langle \cos \alpha(r, t) \rangle$  to plot  $\langle \cos \alpha(r) \rangle$ . To account for collective motions which emerge later in simulations, the time-averaging was done for last 50 s. We set  $\Delta r$  to 0.2  $\mu\text{m}$ , and a maximum distance that we considered for the calculation is 1  $\mu\text{m}$ .

### Quantification of F-actin curvature

Persistence length of F-actin can be calculated directly using the following relationship:

$$l_p = \frac{\kappa_{b,A} r_{0,A}}{k_B T} \quad (3)$$

where  $\kappa_{b,A}$  is the bending stiffness of F-actin in N·m. However, F-actins interacting with motors can have a curvature leading to a different persistence length. We evaluated the actual curvature of F-actin by measuring a correlation between unit tangential vectors along the contour of F-actin,  $\mathbf{u}(s)$ :

$$\langle \cos \theta \rangle = \langle \mathbf{u}(s) \cdot \mathbf{u}(s + \Delta s) \rangle \quad (4)$$

where  $s$  is a position along the contour of F-actin, and  $\Delta s$  is a distance between two positions where the correlation is calculated. This measurement is often used for evaluating the persistence length of polymers.  $\langle \cos \theta \rangle$  is plotted as a function of  $\Delta s$  to evaluate the curvature of F-actins. A faster decrease in  $\langle \cos \theta \rangle$  is indicative of F-actins with a higher curvature.

### Evaluation of network morphology

We evaluated heterogeneity of network morphology by measuring spatial distribution of F-actins. For the measurement, the computational domain is divided into  $N_G \times N_G$  grids in the x and y directions, where  $N_G$  represents the number of grids in each direction. Each grid has its own coordinate,  $(i, j)$ . We measured the number of actin segments located in each grid,  $\rho_A^{i,j}$ . Then, the standard deviation of  $\rho_A^{i,j}$  is calculated over grids with constant  $i$  or  $j$  (i.e. in x or y direction). By averaging all the standard deviations, heterogeneity of F-actin,  $Q_A$ , is calculated like the following:

$$Q_A = \frac{1}{2N_G} \left[ \sum_{i=1}^{N_G} \text{std} \left( \rho_A^{i,j} \Big|_{j=1..N} \right) + \sum_{j=1}^{N_G} \text{std} \left( \rho_A^{i,j} \Big|_{i=1..N} \right) \right] \quad (5)$$

Since the heterogeneity calculated in this method depends on the choice of  $N_G$ , we carefully determined the optimal value of  $N_G$  at 20. We also calculated the time-average of  $Q_A$  for last 50 s to account for network morphology at later times.

In addition, using  $30 \times 30$  grids, we evaluated how network morphology evolves over time in each simulation. We calculated a correlation between  $\rho_A^{i,j}$  in grids at the end of a simulation and  $\rho_A^{i,j}$  in grids at each time point. If network morphology quickly reaches a steady state and does not vary significantly at later times, the correlation also increases fast and then remains near 1 till the end. If network morphology keeps changing over time, the correlation increases gradually. To quantify how dynamically a network changes its morphology, we calculated duration which the correlation is larger than 0.5. Larger duration indicates more static or “frozen” network morphology.

### Analysis of forces on F-actins and motors

We calculated the average of spring forces acting on all chains of F-actins at each time point. It has been shown previously that motor activities induce tensile forces on F-actins

because the compressive forces are relaxed due to buckling. Thus, dominance of tensile forces on F-actins can be an indicator for contractile (i.e. tensile) stress on networks. To show a correlation between local stress and network morphology, we calculated the distribution of spring energy density in a network at the end of a simulation. We divided a computational domain into  $30 \times 30$  grids in the x and y directions. In each grid, we calculated the sum of spring energy of all actin segments and divided the sum by the volume of each grid to obtain spring energy density of each grid in  $\text{J}/\text{m}^3$ . Since most of the F-actins are subjected to tensile forces, the contribution from F-actins under compression to spring energy is negligible. The distribution of spring energy density is visualized using heat maps with color scaling.

In addition, forces exerted by motor arms that are interacting with F-actins were monitored. The average of the forces was calculated over time to estimate how much force motors generated at each time point on average.

### Volume-exclusion effects between F-actins

Repulsive force between F-actins depends on the distance between actin segments and represented by a harmonic potential:

$$U_r = \begin{cases} \frac{1}{2} \kappa_{r,A} (r_{12} - r_{c,A})^2 & \text{if } r_{12} < r_{c,A} \\ 0 & \text{if } r_{12} \geq r_{c,A} \end{cases} \quad (6)$$

where  $\kappa_{r,A}$  is strength of the repulsive force,  $r_{12}$  is a minimum distance between two actin segments, and  $r_{c,A}$  is the diameter of an actin segment.

## RESULTS

### Effects of properties of F-actin and motor

Before investigating roles of volume-exclusion effects and ACPs, it is necessary to determine more basic properties of F-actin and motor. Thus, we tested effects of three parameters in the absence of ACPs (i.e. zero ACP density,  $R_{\text{ACP}} = 0$ ) and volume-exclusion effects ( $\kappa_{\text{r,A}} = 0$ ): average length of F-actin ( $\langle L_f \rangle$ ), motor density ( $R_M$ ), and ATP-dependent unbinding rate of motors ( $k_{20}$ ). Note that without ACPs and volume-exclusion effects, F-actins move independently without physical interactions with other F-actins. For a reference condition,  $\langle L_f \rangle$  is  $\sim 1.5 \mu\text{m}$ ,  $R_M$  is 0.8, and  $k_{20}$  is  $20 \text{ s}^{-1}$ . Under the reference condition, F-actins move relatively fast and quite persistently as observations in the myosin motility assay experiments (Movie S1). We varied one of the three parameters with others fixed in order to evaluate the influences of each parameter.

First, we changed  $R_M$  between 0.008 and 0.8. Note that it is hard to evaluate the dependence of F-actin behaviors on  $R_M$  if models consider motors in an implicit manner. With fewer motors, F-actins move slower and change their directions more often (Figs. 1a and S2a). If motors are sparsely distributed in space, it is much harder for F-actins to maintain connection to motors. Therefore, there are a larger portion of F-actins diffusing without connection to any motor and F-actins bound to only one motor at lower  $R_M$ , resulting in much lower speed and persistency (Fig. 1b). In addition, with fewer motors, a correlation between unit tangential vectors measured along the contour of F-actins deviates more from that corresponding to their persistence length because F-actins may need to bend more to bind to sparsely distributed motors (Fig. S2b). Spatial distribution of F-actins is homogeneous regardless of  $R_M$  (Figs. S2c-d).

Second, we altered  $\langle L_f \rangle$  between  $0.62 \mu\text{m}$  and  $5.06 \mu\text{m}$ . In these cases, we used  $R_M = 0.08$  which is 10-fold smaller than the reference condition because we found that effects of  $\langle L_f \rangle$  with  $R_M = 0.8$  are not significant. With larger  $\langle L_f \rangle$ , the frequency of F-actins moving faster increases (Fig. 1c). Short F-actins are more likely to lose all connections to motors. Then, more F-actins diffuse in space with lower  $\langle L_f \rangle$  (Fig. 1d). In addition, the number of F-actins bound

to only one motor that can move slower due to possible rotation also increases. These F-actins result in tails at low speed in the speed distribution. The range of  $\langle L_f \rangle$  for being these F-actins is determined largely by average distance between adjacent motors fixed in space. With lower  $R_M$ , the average distance increases, so more F-actins move slower. If F-actins are long, they can maintain connectivity to more than one motor despite a long distance between adjacent motors, so the speed can be relatively faster. By contrast, if motors are located very densely, effects of  $\langle L_f \rangle$  become negligible. Longer F-actins tend to be more curved since such F-actins are bound to many of the sparsely distributed motors via bending (Fig. S3b). Despite their higher curvature, longer F-actins tend to move more persistently in one direction at a short timescale because very short F-actins can rotate due to lack of connectivity to motors (Fig. S3a). Regardless of  $\langle L_f \rangle$ , F-actins show quite homogeneous distribution overall (Figs. S3c-d).

Lastly, we varied  $k_{20}$  between  $5 \text{ s}^{-1}$  and  $640 \text{ s}^{-1}$ . As  $k_{20}$  increases, both unbinding and walking rates of motors measured in simulations are higher, consistent with imposed walking ( $k_{w,M}$ ) and unbinding rates ( $k_{u,M}$ ) of motors (Fig. 2a). The enhanced walking rate increases speed of F-actins in general (Fig. 2b). In addition, due to significantly higher unbinding rate, connections between F-actins and motors become very unstable. A higher unbinding rate leads to a lower number of active motors bound to F-actins at equilibrium (Fig. 2c), and F-actins frequently change their directions during movement (Fig. 2d). However, the curvature of F-actin and the heterogeneity of F-actin spatial distribution are not affected by  $k_{20}$  (Figs. S4a-c). F-actins experience slightly larger tensile forces only at lower  $k_{20}$  because motors with high  $k_{20}$  mostly walk at unloaded velocity due to their high unbinding rate (Figs. 2a and S4d).

### **Collective behaviors of F-actins in the presence of volume-exclusion effects**

In simulations described above, we ignored volume-exclusion effects to focus only on interactions between F-actins and myosin motors. However, in the motility assay experiments, F-actins can feel the existence of other F-actins via their physical volumes because F-actins are

located at similar height. The degree of volume-exclusion effects between F-actins can be varied by altering crowding effects that push F-actins down toward a surface coated with myosin motors. Several motility assay experiments have demonstrated the emergence of collective behaviors of F-actins in the presence of strong volume-exclusion effects.<sup>7-11, 14</sup>

We investigated roles of volume-exclusion effects between F-actins in gliding behaviors of F-actins by imposing high repulsive forces ( $\kappa_{r,A} = \kappa_{r,A}^*$ ). It was observed that most of F-actins are aligned with each other when they collide, but they can still cross over each other if they encounter with a very large contact angle. With the reference actin concentration ( $C_A = 60 \mu\text{M}$ ), F-actins form thin bundles soon after they start moving (Fig. 3a and Movie S2, center). These bundles are merged into thicker bundles over time, and some of the bundles form ring-like structures. Some of the ring-like structures last till the end of simulations, whereas the others disappear after some time.

When  $C_A$  is reduced, ring-like structures emerge less frequently, and F-actins move in a more persistent manner and show less curvature because collisions between F-actins occur less frequently at lower  $C_A$  (Figs. 3b, S5a-b and Movie S2, left). At the lowest  $C_A$  ( $15 \mu\text{M}$ ), ring-like structures are not formed anymore, whereas transient formation of bundles still takes place. By contrast, as  $C_A$  increases, thick and long bundles are formed over time. Persistency of F-actin motions decreases, and the curvature of F-actins increases (Figs. 3b, S5a-b, and Movie S2, right). In all cases, there is no significant temporal change in the ensemble average of F-actin speed, indicating consistent motions of F-actins regardless of the frequency of collision events (Fig. S5c). Heterogeneity of network morphology gradually increases and reaches a plateau to a different extent (Fig. S5d). With high  $C_A$ , network morphology does not vary much at later times (Fig. 3c and Movie S2, right). This observation is quite interesting in that the network forms a time-invariant frame along which F-actins can glide dynamically (Movie S2). Due to collision events, it is expected that neighboring F-actins move in a parallel manner in all cases. Indeed, we found that F-actins glide in a collective fashion by measuring

a correlation between velocities of neighboring F-actins (Fig. 3d). Interestingly, the correlation at a distance smaller than  $0.5 \mu\text{m}$  is maximal in a case with  $120 \mu\text{M}$ . In this case, two large, thick ring-like structures are formed by behaving like a “sink” for F-actins; a number of F-actins are sucked into these structures and then trapped (Movie S2, right). In addition, distances between thick bundles and ring-like structures are relatively long. Thus, the correlation becomes very large in this case. With  $C_A = 240 \mu\text{M}$ , the distances become smaller, so the correlation includes many pairs of F-actins located within different bundles or ring-like structures. These F-actins do not necessarily move in the same direction, resulting in a lower correlation than that with  $C_A = 120 \mu\text{M}$ .

We also probed influences of the extent of volume-exclusion effects on motions of F-actins with high  $C_A$  ( $= 120 \mu\text{M}$ ) by varying the strength of repulsive forces acting between neighboring pairs of F-actins ( $\kappa_{r,A}$ ). With 3-fold lower  $\kappa_{r,A}$ , ring-like structures are not formed anymore (Fig. 4a and Movie S3, left). Bundle-like structures still emerge, but bundle formation is not as clear as that in the reference case. With 10-fold lower  $\kappa_{r,A}$ , bundle formation is not obvious, becoming closer to cases without volume-exclusion effects shown earlier. By contrast, with 3-fold higher  $\kappa_{r,A}$ , a large number of ring-like structures are formed (Movie S3, right). Thus, with higher  $\kappa_{r,A}$ , network morphology tends to be more heterogeneous (Figs. 4a-b and S6a). The frozen network morphology emerging at later times is more apparent with higher  $\kappa_{r,A}$  (Figs. 4c and S6b). At  $C_A \leq 60 \mu\text{M}$ , the correlation between velocities of neighboring F-actins is higher with larger  $\kappa_{r,A}$ , meaning that collective behaviors of F-actins are determined by the extent of volume-exclusion effects at lower actin concentration (Figs. S6c-d). However, at  $C_A = 120 \mu\text{M}$ , the correlation becomes maximal with the reference value of  $\kappa_{r,A}$ . Thick bundles and large ring-like structures in the case explained above lead to a higher correlation than many of smaller ring-like structures.

The dependence of F-actin motions and network morphology on volume-exclusion effects can be explained by what happens to F-actins when they encounter at a large or small

contact angle. If volume-exclusion effects are very weak, F-actins cross over each other with a slight change in their gliding direction caused by weak repulsive forces (Fig. 4d, left). With relatively strong volume-exclusion effects, F-actins can align with each other if they encounter with a small contact angle, but they cross over each other if the angle is large (Fig. 4d, center). This behavior can lead to the formation of thick, large bundles by allowing F-actins to move at longer distances until they encounter other F-actins with similar orientations. If the volume-exclusion effects are very strong, F-actins cannot cross over each other regardless of the contact angle (Fig. 4d, right). This results in a frequent change in their gliding directions and higher curvature, leading to the formation of ring-like structures.

### Impacts of the density and unbinding rate of ACPs

Most of the traditional motility assay experiments were performed without ACPs that cross-link pairs of F-actins. More recently, several experiments demonstrated how different types of ACPs lead to distinct network morphology and F-actin movements at very high actin concentration ( $C_A$ ).<sup>12-14</sup> In addition, a myriad of experimental and computational studies have demonstrated that the amount of ACPs highly affects the contraction of actomyosin networks with myosin thick filaments (i.e. mobile motors).<sup>21, 31, 32</sup> It is expected that even with lower  $C_A$  and immobile motors, the density and property of ACPs will still regulate contractile behaviors of networks. Among various ACP properties, we focus on the unbinding rate of ACPs that is expected to vary, depending on types of ACPs. For example, while scruin is known to form permanent cross-links between F-actins,<sup>33</sup> most of the ACPs unbind from F-actins at distinct force-dependent rates.<sup>34</sup> We evaluated effects of density ( $R_{ACP}$ ) and zero-force unbinding rate constant ( $k_{u,ACP}^0$ ) of ACPs by varying them over wide ranges:  $0.001 \leq R_{ACP} \leq 0.1$  and  $0 \leq k_{u,ACP}^0 / k_{u,ACP}^{0*} \leq 10$ , where  $k_{u,ACP}^{0*} = 0.115 \text{ s}^{-1}$  is a reference value of  $k_{u,ACP}^0$ . We did not include repulsive forces between F-actins in these simulations.

We observed that F-actins move slower and change their directions more frequently with higher  $R_{ACP}$  than those with lower  $R_{ACP}$  (Figs. 5a and S7a-b). This suggests that ACPs prevent F-actins from persistently moving via formation of cross-linking points between F-actins. If  $k_{u,ACP}^0$  is increased with  $R_{ACP}$  fixed, the fraction of ACPs in an active state (i.e. bound to a pair of F-actins) is reduced (Fig. S8a), and also it becomes much easier for motors to displace F-actins because each cross-linking point exerts lower effective friction to F-actin due to more frequent unbinding events. Because of these two effects, F-actins move faster and more persistently with higher  $k_{u,ACP}^0$  (Figs. 5a and S7a-b). In addition, in a case with  $R_{ACP} = 0.03$  and  $k_{u,ACP}^0 = 0$ , the average speed of F-actins is nearly zero (Fig. 5a), indicating that ACPs corresponding to  $\sim 3\%$  of actins are sufficient enough to cross-link all F-actins into a network at  $C_A = 60 \mu\text{M}$ .

Network morphology exhibits interesting dependence on  $R_{ACP}$  and  $k_{u,ACP}^0$  (Figs. 5b-c and S7c). If there is no ACP unbinding ( $k_{u,ACP}^0 = 0$ ), the heterogeneity of network morphology is slightly higher at  $R_{ACP} = 0.003-0.03$ . In addition, at this range of  $R_{ACP}$ , F-actins experience the largest tensile force (Figs. S7d and S8b). If ACPs form permanent cross-linking points, two populations of F-actins exist: cross-linked population and free population. Note that the latter hardly affects heterogeneity of network morphology because they do not aggregate as shown earlier in cases without ACPs. Due to the absence of unbinding, there is no change in states of F-actins over time. Thus, in this case,  $R_{ACP}$  determines the number of F-actins in the two populations. If a network is cross-linked too loosely ( $R_{ACP} = 0.001$ ), most F-actins glide on motors freely at speed close to the unloaded walking speed of motors (Fig. 5a), leading to homogeneous F-actin spatial distribution (Fig. 5b). Accordingly, tensile forces acting on F-actins and those exerted by motors are quite low (Figs. S7d and S8b-c). By contrast, if F-actins in a network are cross-linked too heavily ( $R_{ACP} > 0.01$ ), most of F-actins cannot move far from their initial locations as seen in nearly zero average speed (Fig. 5a), resulting in relative

homogeneous morphology (Figs. 5b-c). In addition, although forces generated by motors are similar in all cases with  $R_{ACP} > 0.001$ , net tensile forces acting on F-actins are smaller with  $R_{ACP} = 0.1$  since much larger motor forces are required for buckling of short segments between numerous cross-linking points (Figs. S7d and S8b-c). Thus, under these two extreme conditions with high and low  $R_{ACP}$ , motors are not able to aggregate F-actins or generate large net tensile forces on F-actins. However, at intermediate level of  $R_{ACP}$ , motors can deform a network consisting of F-actins cross-linked relatively well by generating larger tensile forces originating from F-actin buckling.

If ACPs can unbind from F-actins (i.e.  $k_{u,ACP}^0 > 0$ ), highly heterogeneous networks with several clusters are observed because F-actins can be displaced significantly (Figs. 5b-c, S7c and Movie S4). Such high heterogeneity appears at a specific range of density of active ACPs,  $\sim 0.005 \leq R_{ACP}^{active} \leq \sim 0.05$  (Fig. S8a), where  $R_{ACP}^{active}$  is the density of active ACPs, equal to the fraction of active ACPs times  $R_{ACP}$  (Fig. S8a). Interestingly, the average tensile force exerted on F-actins tends to be proportional to  $R_{ACP}$ , unlike cases without ACP unbinding (Figs. S7d and S8b). Only one case ( $R_{ACP} = 0.1$  and  $k_{u,ACP}^0 / k_{u,ACP}^{0*} = 0.01$ ) that exhibits less heterogeneous F-actin spatial distribution shows sustainable tensile force on F-actins (Figs. S7c-d). This is attributed to small loads on each ACP and stable cross-linking points with large effective friction (Movie S5). This implies that tensile stress in the presence of ACP unbinding is generated and sustained only in these networks when most of F-actins are cross-linked stably. By contrast, in all other cases, average tensile forces acting on F-actins reach a peak and then relax to non-zero asymptote. Both peak and equilibrium levels are inversely proportional to  $k_{u,ACP}^0$ .

Spring energy density in networks tends to be proportional to  $R_{ACP}$  but inversely proportional to  $k_{u,ACP}^0$  in general (Fig. S8d), which is consistent with our previous study<sup>21</sup>. If  $k_{u,ACP}^0$  is very small, and if  $R_{ACP}$  is very high, similar levels of spring energy emerge across the network because almost all F-actins are cross-linked stably throughout the network as seen in

very homogeneous network morphology (Figs. 5b-c). By contrast, in cases where a network aggregates into clusters, high spring energy is concentrated mostly on the clusters since the clusters are not connected to each other (Figs. 5c and S8d).

## DISCUSSION

Since the 1980s, the *in vitro* motility assay has been used to study interactions between F-actins and myosin motors. By measuring gliding motions of a few F-actins propelled by myosin motors fixed on a surface, several properties of myosin motors, such as duty ratio and mechanochemical cycles, have been estimated.<sup>30, 35</sup> The system of *in vitro* myosin motility assay has advanced recently. When F-actin concentration was significantly increased with strong crowding effects, interesting collective motions of F-actins were observed.<sup>6</sup> In addition, inclusion of different types of ACPs resulted in formation of distinct structures.<sup>13</sup> Compared to experimental efforts, the motility assay has not been studied very actively via a computational model although a rigorous model can provide more insights than experiments. In this study, we investigated motions of F-actins in the motility assay, using our well-established agent-based computational model.

First, we investigated motions of F-actins without ACPs and volume-exclusion effects between F-actins. We showed how the average length of F-actin and the density and mechanochemical rate of motors affect motions of F-actins. Morphology of the network was very homogeneous in all cases regardless of a change in those parameters. However, it was observed that F-actins may move with different speed, persistency, and curvature depending on the properties of F-actin and motor. In particular, if continuous interactions between motors and F-actins are hindered due to either large spacing between motors or short filament length, many of F-actins cannot glide at speed close to the unloaded walking velocity of motors (Fig. 1). Indeed, other *in vitro* study showed that F-actins move slower at low motor density,<sup>36</sup>

and a computational study also showed that the movement of F-actins is much slower and less persistent if motor density is too low because the number of myosin heads bound to F-actins at a given time becomes too low.<sup>17</sup> By contrast, in experiments and simulations performed with long F-actins and high motor density (i.e. small spacing between motors), the dependence on motor density and F-actin length has not been observed. For example, an in vitro study showed that the gliding speed of F-actin hardly depends on the length of F-actin varied between  $\sim 1 \mu\text{m}$  and  $\sim 17 \mu\text{m}$  with motor density of  $\sim 600 \text{ motors}/\mu\text{m}^2$ .<sup>37</sup> If these motors are uniformly distributed on a surface, average spacing between them is  $\sim 42 \text{ nm}$ . In addition, a computational study reported that F-actin motility is independent of motor density varied between  $\sim 1,500$  and  $\sim 6,000 \text{ motors}/\mu\text{m}^2$  which corresponds to average spacing of  $\sim 13 \text{ nm}$  to  $\sim 26 \text{ nm}$ .<sup>18</sup> Under such high motor density, spacing between motors is much shorter than F-actins, so F-actins are likely to be bound to several motors unless F-actins are extremely short. In contrast to these studies, we reduced motor density substantially and found that the gliding speed of F-actins can depend significantly on F-actin length with motor density corresponding to average spacing of  $\sim 0.33 \mu\text{m}$  ( $R_M = 0.08$ ). We also observed that dependence of the gliding speed on F-actin length is much weaker if motor density is 10-fold higher (data not shown). It is anticipated that dependence of F-actin gliding speed on F-actin length will be also observed in experiments if motor density is lowered significantly.

We also found that the gliding speed of F-actin shows biphasic dependence on one of the mechanochemical rates, the ATP-dependent unbinding rate (Fig. 2). As the rate increases, motors walk on F-actin faster and are detached from F-actin more frequently. As long as walking takes place more frequently than detachment from F-actin, the gliding speed of F-actins also increases in proportion to an increase in the ATP-dependent unbinding rate. However, if the rate becomes too high, detachment from F-actin dominates walking, resulting in lower net gliding speed of F-actin than walking speed of motors. It is expected that a discrepancy between the gliding speed of F-actins and walking speed will be less even with

very high ATP-dependent unbinding rate if F-actins are very long, or if motor density is very high as in experiments. As long as F-actins can interact with a few motors at each time point, F-actins can keep moving without significant delay even with a small duty ratio. This is reminiscent of a strategy that a thick filament consisting of skeletal muscle myosin motors with a very small duty ratio employs to stay on F-actins.<sup>30</sup> Indeed, previous computational<sup>18</sup> and in vitro studies<sup>29, 36</sup> with high motor density showed that F-actin gliding speed increases with higher ATP concentration and reaches a plateau, rather than showing a biphasic dependence on ATP concentration. This can be attributed to higher motor density used in the previous experiments<sup>36</sup> ( $\sim 150$  motors / $\mu\text{m}^2$  which corresponds to average spacing of  $\sim 81$  nm) and simulations<sup>18</sup> ( $\sim 1,500$  to  $\sim 6,000$  motors / $\mu\text{m}^2$  which corresponds to average spacing of  $\sim 13$ - $26$  nm) than that used in our simulation ( $R_M = 0.008$  to  $R_M = 0.8$  which corresponds to average spacing of  $\sim 0.11$   $\mu\text{m}$  to  $\sim 1.1$   $\mu\text{m}$ ). In addition, longer F-actin used in the previous experiments and simulations can prevent the gliding speed from decreasing at high ATP concentration. If these simulations and experiments are repeated with much lower motor density and shorter F-actins, the biphasic dependence of F-actin speed on ATP concentration would emerge.

Then, we showed volume-exclusion effects between F-actins affect motions of F-actins in the motility assay, thus resulting in bundles or ring-like structures (Figs. 3 and 4). If F-actins are aligned only when they encounter other F-actin at a small contact angle due to low  $\kappa_{r,A}$ , large, thick bundles are formed at high actin concentration. If F-actins are aligned with other F-actin at most of the collision events regardless of a contact angle due to high repulsive force, small ring-like structures dominantly emerge. Once the bundles and ring-like structures are formed in our simulations, network morphology does not change significantly over time. However, the thick bundles are comprised of consistently moving F-actins that enter, leave, or stay within the structures (Movies S2 and S3). It means that the system reached a steady state at network level in terms of morphology, but it is still very dynamic at filament

level. However, if actin concentration becomes lower, F-actins transiently form thin bundles, resulting in a dynamic change in network morphology over time.

Formation of bundles has been suggested in previous studies where volume-exclusion effects between F-actins were modulated by varying concentration of crowding agents, such as methylcellulose (MC) and polyethylene glycol (PEG). With higher MC concentration, F-actins showed collective motions and formed bundles and ring-like structures at larger length-scales.<sup>6, 38</sup> It was also shown that F-actins move in a bidirectional manner along bundles, implying a dynamic steady state.<sup>38</sup> However, formation of small ring-like structures has not been observed in previous experiments. If motility assay experiments are performed with very strong crowding effects and lower motor density, small ring-like structure may emerge. Emergence of large-scale flow of numerous F-actins was shown in other experiments.<sup>7-11</sup> The flow is initiated from seeds with a few F-actins, and the seeds gradually increase in size over time, becoming clusters with the large-scale flow.<sup>10</sup> These clusters are also in a dynamic steady state, maintaining relatively constant size by continuously losing and recruiting F-actins.<sup>10</sup> Because we employed a small computational domain ( $10 \times 10 \times 0.1 \mu\text{m}$ ) and short F-actins, it is not likely to recapitulate such large dynamics structures. It is feasible to simulate a large system with long F-actins for directly comparing simulation results with experimental observations, by imposing a more computational resource to each simulation. However, it is beyond the scope of this study. In a future study, we will attempt to simulate large-scale dynamic structures and analyze collective behaviors of F-actins in greater depth.

Interestingly, it was reported in a recent study that F-actins form steady-state thick bundle structures even without myosins if crowding effects are strong.<sup>6</sup> In this study, F-actins are displaced because they grow rapidly from a surface via formin activities. Similarity in results implies that F-actins at high density can form the thick bundles as long as they keep moving somehow in the presence of strong volume-exclusion effects. In addition, collective behaviors were observed in experiments performed in a different setup. The ring-like

structures were shown in an experiment with ACPs called fascin, and they were named “frozen steady states”<sup>14</sup>. Note that we observed them in simulations without any ACP, but they are much smaller than those observed in the experiment that are as large as  $\sim 30 \mu\text{m}$  in radius. We would be able to reproduce large-scale rings with both volume-exclusion effects and ACPs that connect only parallel F-actins, but this is beyond the scope of the current study. A computational study demonstrated that volume-exclusion effects between microtubules result in ordered structures composed of bundles.<sup>39</sup> In addition, formation of ring-like structures and large-scale collective behaviors of microtubule were observed due to physical interactions between microtubules.<sup>40-42</sup>

Lastly, we showed that inclusion of ACPs in a network without volume-exclusion effects between F-actins can significantly enhance the spatial heterogeneity of network morphology (Fig. 5). If there are too many ACPs, or if the unbinding rate of ACPs is too low, motors cannot readily break cross-linking points, resulting in a homogenous network with frozen or slowly moving F-actins. By contrast, if there are only a few ACPs, or if ACPs unbind from F-actins very frequently, F-actins move mostly freely due to unstable cross-linking points that can break by applied loads, leading to a homogenous network. At intermediate density and unbinding rate of ACPs, networks become quite heterogeneous because both good connectivity between F-actins and deformability via breakage of cross-linking points are achieved. A fraction of the weak cross-linking points break due to applied forces while the other stable ones keep holding pairs of F-actins. Note that an increase in the amount of ACPs or a decrease in the unbinding rate of ACPs results in a larger number of active ACPs bound to two F-actins at dynamic equilibrium, but there is a difference between the two cases. Even if two systems have the same amount of active ACPs at dynamic equilibrium, F-actins in a system with higher ACP unbinding rate can move faster because more transient cross-linking points lead to lower effective friction between two cross-linked F-actins.

This overall observation is consistent with previous studies showing the highest contractility of networks at intermediate density of ACPs.<sup>12, 13, 22, 31, 43</sup> A network cross-linked by ACPs in our model became heterogeneous only above the critical amount of active ACPs that corresponds to a percolation threshold, as suggested by.<sup>44, 45</sup> If there are too many active ACPs, contraction was reduced because buckling of F-actin is suppressed, which is consistent with the importance of buckling for contraction suggested by previous studies.<sup>46-48</sup> In addition, emergences of clusters at lower ACP density and meshes at higher ACP density are consistent with results of previous simulations for cytokinetic rings although we did not observe ring formation at intermediate ACP density due to immobile motors.<sup>49</sup>

## CONCLUSIONS

In this study, we proposed a computational model designed for simulating myosin motility assays in a more rigorous fashion than previous models. The model successfully recapitulated previous experimental observations and also showed new interesting behaviors of F-actins under various conditions. We demonstrated effects of each parameter on behaviors of F-actins and networks by varying values of many parameters beyond the capability of experiments. In particular, volume-exclusion effects and ACPs play a very important role in the motions of F-actins and network morphology. In the near future, we will simulate the motility assay system in the presence of both volume-exclusion effects and ACPs. In addition, using the power and flexibility of our model, we will simulate a larger system for direct comparison with in vitro experiments as well as a motility assay with microtubules and kinesin motors that were employed in many recent studies.

## ACKNOWLEDGMENTS

The authors gratefully acknowledge the supports from the National Institutes of Health (1R01GM126256) and the support from JST CREST (JPMJCR14W2). This work used the Extreme Science and Engineering Discovery Environment (XSEDE)<sup>50</sup>, which is supported by National Science Foundation grant number ACI-1548562. The computations were conducted on the Comet supercomputer, which is supported by NSF award number ACI-1341698, at the San Diego Supercomputing Center (SDSC).

## REFERENCES

1. M. L. Gardel, K. E. Kasza, C. P. Brangwynne, J. Liu and D. A. Weitz, *Methods Cell Biol.*, 2008, **89**, 487-519.
2. M. Murrell, P. W. Oakes, M. Lenz and M. L. Gardel, *Nature reviews. Molecular cell biology*, 2015, **16**, 486-498.
3. M. Schliwa and G. Woehlke, *Nature*, 2003, **422**, 759-765.
4. J. A. Spudich, *Nature reviews. Molecular cell biology*, 2001, **2**, 387-392.
5. T. Butt, T. Mufti, A. Humayun, P. B. Rosenthal, S. Khan and J. E. Molloy, *J. Biol. Chem.*, 2010, **285**, 4964-4974.
6. T. Iwase, Y. Sasaki and K. Hatori, *Biochim. Biophys. Acta.*, 2017, **1861**, 2717-2725.
7. V. Schaller and A. R. Bausch, *Proc. Natl. Acad. Sci. U. S. A.*, 2013, **110**, 4488-4493.
8. V. Schaller, C. Weber, E. Frey and A. R. Bausch, *Soft Matter*, 2011, **7**, 3213-3218.
9. V. Schaller, C. Weber, C. Semmrich, E. Frey and A. R. Bausch, *Nature*, 2010, **467**, 73-77.
10. R. Suzuki and A. R. Bausch, *Nat. Commun.*, 2017, **8**, 41.
11. R. Suzuki, C. A. Weber, E. Frey and A. R. Bausch, *Nat. Phys.*, 2015, **11**, 839-843.
12. V. Schaller, B. Hammerich and A. R. Bausch, *Eur. Phys. J. E Soft Matter*, 2012, **35**, 81.
13. V. Schaller, K. M. Schmoller, E. Karakose, B. Hammerich, M. Maier and A. R. Bausch, *Soft Matter*, 2013, **9**, 7229-7233.

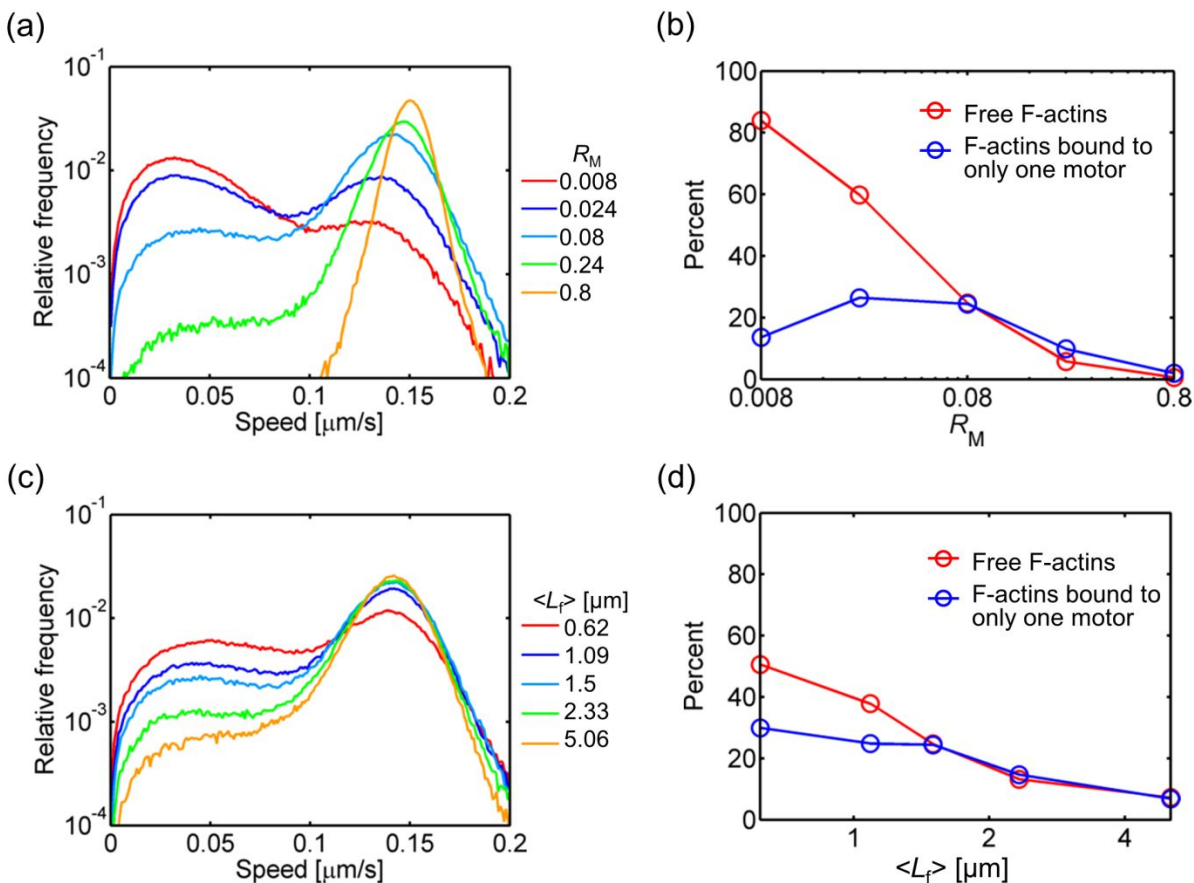
14. V. Schaller, C. A. Weber, B. Hammerich, E. Frey and A. R. Bausch, *Proc. Natl. Acad. Sci. U. S. A.*, 2011, **108**, 19183-19188.
15. A. Vilfan, *Biophys. J.*, 2009, **97**, 1130-1137.
16. P. Egan, J. Moore, C. Schunn, J. Cagan and P. LeDuc, *PLoS Comput. Biol.*, 2015, **11**, e1004177.
17. S. L. Freedman, S. Banerjee, G. M. Hocky and A. R. Dinner, *Biophys. J.*, 2017, **113**, 448-460.
18. Y. Ishigure and T. Nitta, *IEEE Trans. Nanobioscience*, 2015, **14**, 641-648.
19. T. Kim, *Biomech. Model. Mechanobiol.*, 2015, **14**, 345-355.
20. T. C. Bidone, W. Jung, D. Maruri, C. Borau, R. D. Kamm and T. Kim, *PLoS Comput. Biol.*, 2017, **13**, e1005277.
21. W. Jung, M. P. Murrell and T. Kim, *Comput. Part. Mech.*, 2015, **2**, 317-327.
22. J. Li, T. Biel, P. Lomada, Q. Yu and T. Kim, *Soft Matter*, 2017, **13**, 3213-3220.
23. G. I. Bell, *Science*, 1978, **200**, 618-627.
24. T. Erdmann, P. J. Albert and U. S. Schwarz, *J. Chem. Phys.*, 2013, **139**, 175104.
25. T. Erdmann and U. S. Schwarz, *Phys. Rev. Lett.*, 2012, **108**, 188101.
26. B. Guo and W. H. Guilford, *Proc. Natl. Acad. Sci. U. S. A.*, 2006, **103**, 9844-9849.
27. W. E. Thomas, V. Vogel and E. Sokurenko, *Annu. Rev. Biophys.*, 2008, **37**, 399-416.
28. G. Cuda, E. Pate, R. Cooke and J. R. Sellers, *Biophys. J.*, 1997, **72**, 1767-1779.
29. S. Umemoto and J. R. Sellers, *J. Biol. Chem.*, 1990, **265**, 14864-14869.
30. D. E. Harris and D. M. Warshaw, *J. Biol. Chem.*, 1993, **268**, 14764-14768.
31. P. M. Bendix, G. H. Koenderink, D. Cuvelier, Z. Dogic, B. N. Koeleman, W. M. Briehner, C. M. Field, L. Mahadevan and D. A. Weitz, *Biophys. J.*, 2008, **94**, 3126-3136.
32. G. H. Koenderink, Z. Dogic, F. Nakamura, P. M. Bendix, F. C. MacKintosh, J. H. Hartwig, T. P. Stossel and D. A. Weitz, *Proc. Natl. Acad. Sci. U. S. A.*, 2009, **106**, 15192-15197.

33. M. L. Gardel, J. H. Shin, F. C. MacKintosh, L. Mahadevan, P. Matsudaira and D. A. Weitz, *Science*, 2004, **304**, 1301-1305.
34. J. M. Ferrer, H. Lee, J. Chen, B. Pelz, F. Nakamura, R. D. Kamm and M. J. Lang, *Proc. Natl. Acad. Sci. U. S. A.*, 2008, **105**, 9221-9226.
35. T. Q. Uyeda, S. J. Kron and J. A. Spudich, *J. Mol. Biol.*, 1990, **214**, 699-710.
36. E. P. Debold, M. A. Turner, J. C. Stout and S. Walcott, *Am. J. Physiol. Regul. Integr. Comp. Physiol.*, 2011, **300**, R1401-R1408.
37. Y. Y. ToYOSHIMA, S. J. Kron and J. A. Spudich, *Proc. Natl. Acad. Sci. U. S. A.*, 1990, **87**, 7130-7134.
38. K. Ozawa, H. Taomori, M. Hoshida, I. Kunita, S. Sakurazawa and H. Honda, *Biophys. Physicobiol.*, 2019, **16**, 1-8.
39. J. Rickman, F. Nédélec and T. Surrey, *Phys. Biol.*, 2019, **16**, 046004.
40. Y. Sumino, K. H. Nagai, Y. Shitaka, D. Tanaka, K. Yoshikawa, H. Chaté and K. Oiwa, *Nature*, 2012, **483**, 448.
41. S. Wada, A. M. R. Kabir, M. Ito, D. Inoue, K. Sada and A. Kakugo, *Soft Matter*, 2015, **11**, 1151-1157.
42. D. Inoue, B. Mahmot, A. M. R. Kabir, T. I. Farhana, K. Tokuraku, K. Sada, A. Konagaya and A. Kakugo, *Nanoscale*, 2015, **7**, 18054-18061.
43. J. M. Belmonte, M. Leptin and F. Nedelec, *Mol. Syst. Biol.*, 2017, **13**, 941.
44. J. Alvarado, M. Sheinman, A. Sharma, F. C. MacKintosh and G. H. Koenderink, *Nat. Phys.*, 2013, **9**, 591-597.
45. J. Alvarado, M. Sheinman, A. Sharma, F. C. MacKintosh and G. H. Koenderink, *Soft Matter*, 2017, **13**, 5624-5644.
46. M. P. Murrell and M. L. Gardel, *Proc. Natl. Acad. Sci. U. S. A.*, 2012, **109**, 20820-20825.
47. M. Lenz, *Phys. Rev. X*, 2014, **4**, 041002.
48. M. Lenz, T. Thoresen, M. L. Gardel and A. R. Dinner, *Phys. Rev. Lett.*, 2012, **108**,

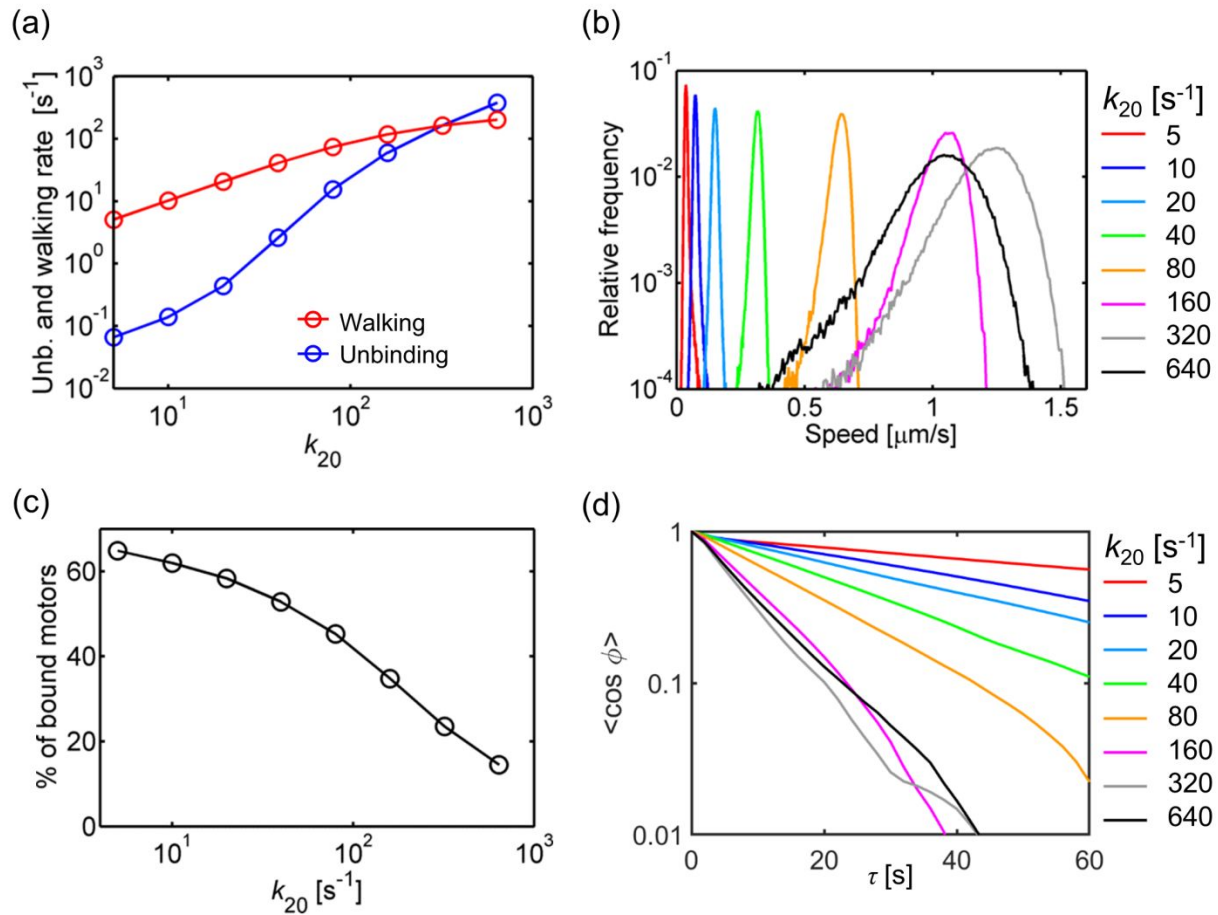
238107.

49. D. Laporte, N. Ojic, D. Vavylonis and J.-Q. Wu, *Mol. Biol. Cell*, 2012, **23**, 3094-3110.
50. J. Towns, T. Cockerill, M. Dahan, I. Foster, K. Gaither, A. Grimshaw, V. Hazlewood, S. Lathrop, D. Lifka and G. D. Peterson, *Comput. Sci. Eng.*, 2014, **16**, 62-74.

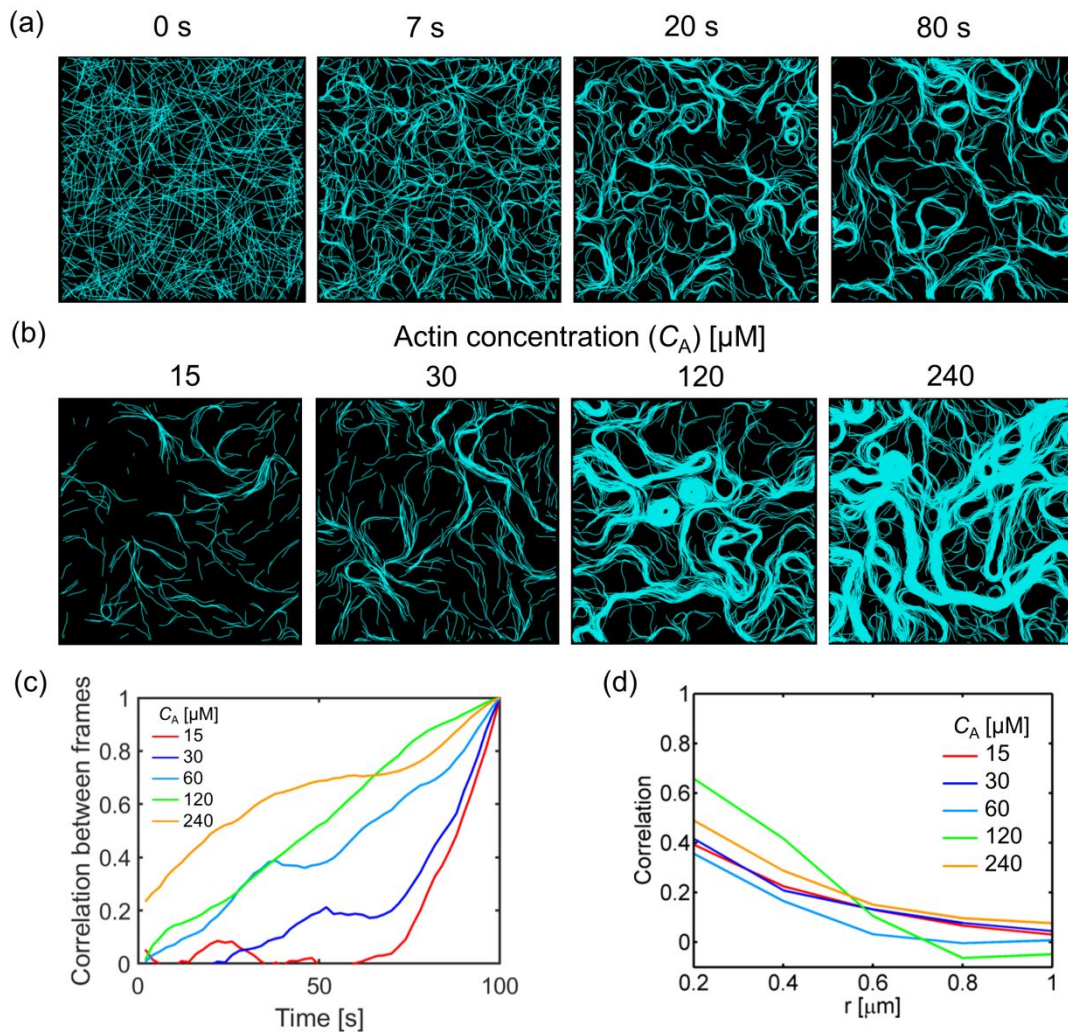
## FIGURES



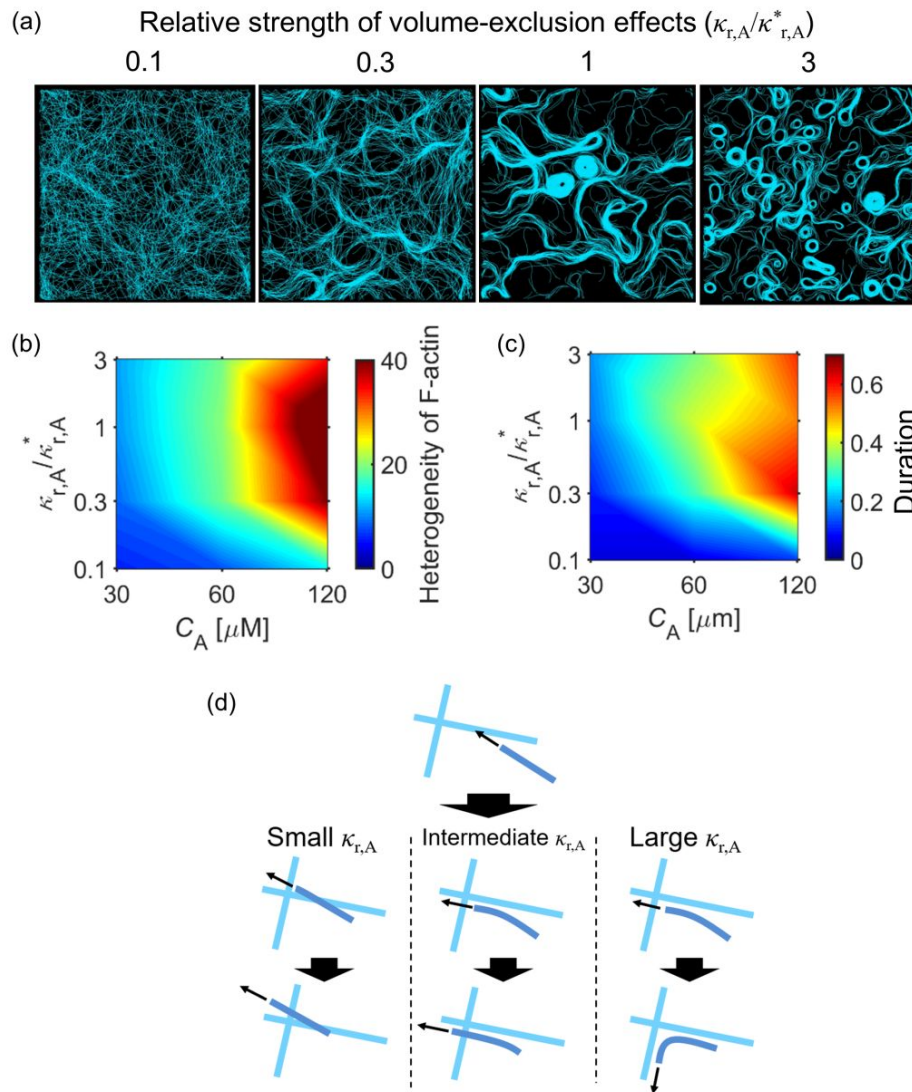
**Figure 1. Motor density ( $R_M$ ) and average length of F-actins ( $\langle L_f \rangle$ ) affect the gliding speed of F-actins.** (a, c) Distribution of speed of F-actins. (b, d) Fraction of F-actins that are bound to only one motor or not bound to any motor. In these cases, volume-exclusion effects between F-actins were not incorporated. With smaller  $R_M$  or  $\langle L_f \rangle$ , speed of F-actin tends to be lower due to a larger number of free F-actins and F-actins bound to only one motor. If F-actins are long enough compared to average spacing between adjacent motors determined by  $R_M$ , most F-actins can keep moving at speed close to the unloaded walking speed of motors ( $\sim 0.14 \mu\text{m/s}$ ).



**Figure 2. A mechanochemical rate in the cross-bridge cycle of myosin motors has a great effect on gliding motions of F-actins.** We varied one of mechanochemical rates of myosin heads employed in the parallel cluster model, the ATP-dependent unbinding rate of motors ( $k_{20}$ ). In these cases, volume-exclusion effects between F-actins were not included. (a) Unbinding and walking rates of motors measured from simulations. (b) Distribution of speed of F-actins. (c) Fraction of active motors that are bound to F-actins. With higher  $k_{20}$ , F-actins tend to move faster, but the speed is reduced at the highest  $k_{20}$  because the unbinding rate of motors is too high for the motors to walk stably on F-actins. (d) Autocorrelation of velocities of F-actins with various  $k_{20}$ . F-actins propelled by motors with higher  $k_{20}$  move much faster and therefore change directions more frequently during the same time interval.

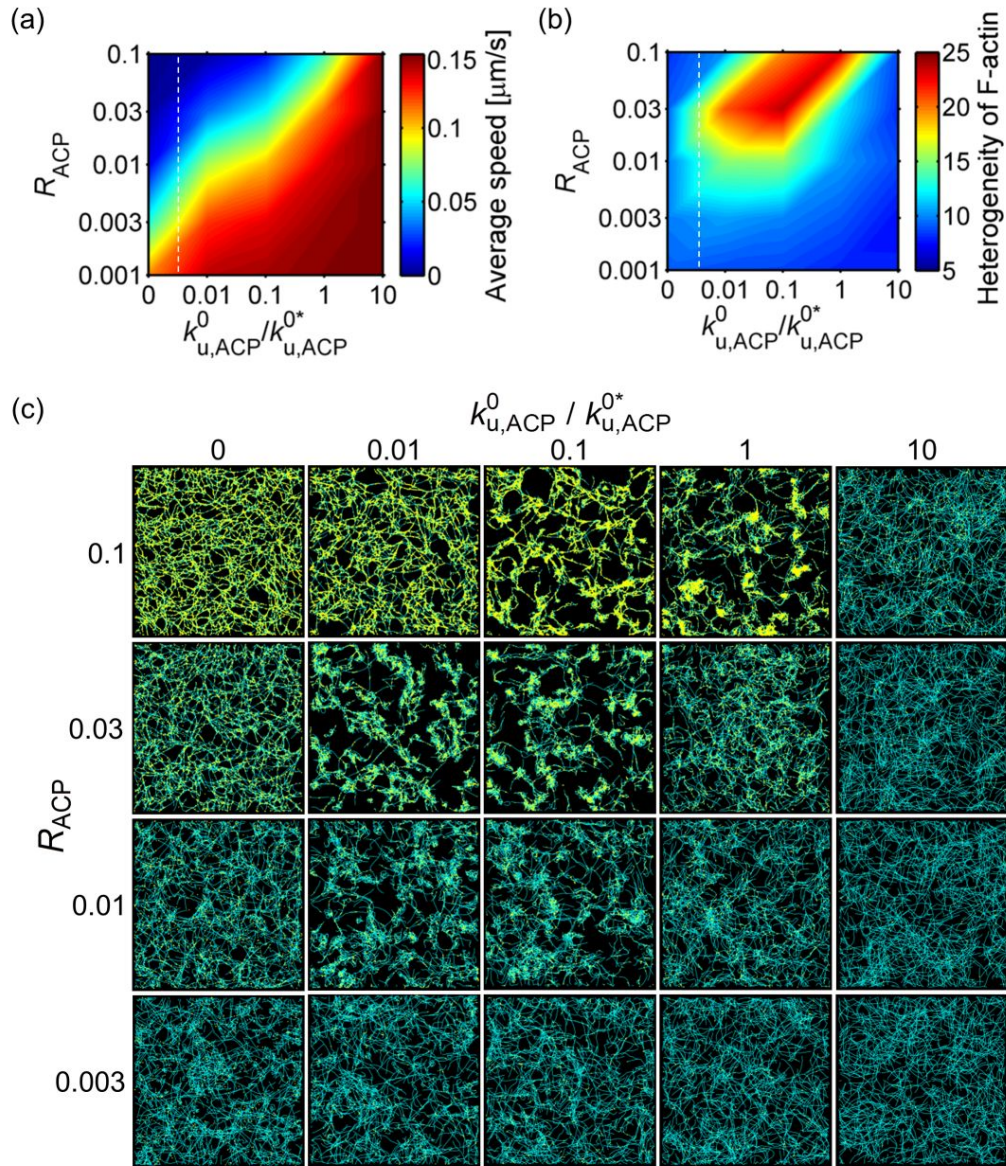


**Figure 3. Volume-exclusion effects between F-actins lead to collective motions of F-actins.** Actin concentration ( $C_A$ ) is varied with reference strength of repulsive forces ( $\kappa_{r,A} / \kappa_{r,A}^* = 1$ ). (a) Time evolution of network morphology with  $C_A = 60 \mu\text{M}$ . Thin bundles emerge first, and then thick bundles and ring-like structures are formed later. (b) Final network morphology with different  $C_A$ . (c) A correlation between network morphology at the end of simulations (100 s) and that at each time point. For example, a correlation value at 50 s represents a correlation between network morphology at 50 s and that at 100 s. Higher correlation values at later times in cases with large  $C_A$  indicate that network morphology does not change significantly near the end. (d) A correlation between velocities of pairs of endpoints on F-actins located at a distance  $r$ , which is averaged for last 50 s.



**Figure 4. The extent of volume-exclusion effects between F-actins highly affects network morphology.** The strength of repulsive forces ( $\kappa_{r,A}$ ) is varied. (a) Final network morphology with different  $\kappa_{r,A}$  at  $C_A = 120 \mu\text{M}$ . With stronger volume-exclusion effects, more ring-like structures appear. (b) Heterogeneity of final network morphology, (c) Duration during which a correlation between final network morphology and morphology at a time point is larger than 0.5, depending on  $C_A$  and  $\kappa_{r,A}$ . With larger  $\kappa_{r,A}$ , network morphology becomes more heterogeneous and does not change much at later times. Effects of  $\kappa_{r,A}$  are weaker if  $C_A$  is smaller. (d) A schematic diagram showing differences in behaviors of F-actins after collisions with other F-actins. If volume-exclusion effects are very weak, F-actins cross over each other easily. If volume-exclusion effects are relatively strong, F-actins can align with each other if a contact angle at the moment of collision is small. However, they cross over each other if the angle is large. This behavior results in formation of thick, large bundles. With very strong

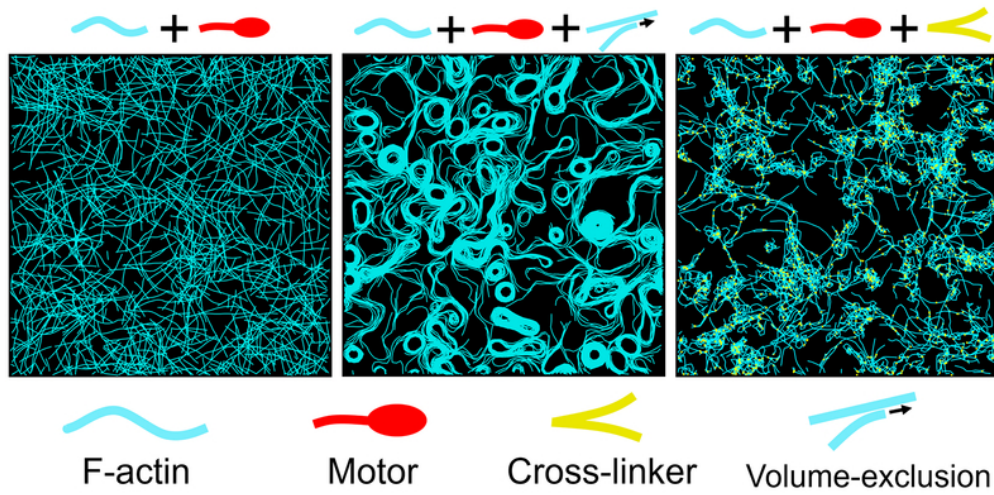
volume-exclusion effects, F-actins cannot cross over each other regardless of whether the contact angle is large or small. Such a frequent change in the direction leads to formation of many, small ring-like structures.



**Figure 5.** Motions and properties of F-actins drastically change depending on density ( $R_{\text{ACP}}$ ) and zero-force unbinding rate constant ( $k_{\text{u,ACP}}^0$ ) of ACPs. (a) Average speed of F-actin averaged for last 50 s and (b) heterogeneity of F-actin spatial distribution measured at the end with various  $R_{\text{ACP}}$  and  $k_{\text{u,ACP}}^0$ . (c) Network morphology measured in all cases at the last time point,  $t = 100$  s. F-actins and ACPs are visualized by cyan and yellow, respectively.  $k_{\text{u,ACP}}^{0*} = 0.115 \text{ s}^{-1}$  is the reference value of  $k_{\text{u,ACP}}^0$ . White dashed lines in (a-b) are drawn to include cases with

$k_{u,ACP}^0 = 0$  in a log scale, so there is a discontinuity between cases with  $k_{u,ACP}^0/k_{u,ACP}^{0*} = 0$  and those with  $k_{u,ACP}^0/k_{u,ACP}^{0*} = 0.01$ . With higher  $R_{ACP}$  and lower  $k_{u,ACP}^0$ , F-actins move slower. Networks become quite heterogeneous at intermediate values of  $R_{ACP}$  and  $k_{u,ACP}^0$ .

# Myosin Motility Assay



66x39mm (300 x 300 DPI)